Plateau Rayleigh instability of soft elastic solids. Effect of compressibility on pre and post bifurcation behavior

Berkin Dortdivanlioglu[a,b,*], Ali Javili[c]

[a] Department of Civil, Architectural and Environmental Engineering, The University of Texas at Austin, Austin, TX 78712, USA
[b] Oden Institute for Computational Engineering and Sciences, The University of Texas at Austin, Austin, TX 78712, USA
[c] Department of Mechanical Engineering, Bilkent University, 06800 Ankara, Turkey

---

Abstract

Solid surface tension can deform soft elastic materials at macroscopic length scales. At a critical surface tension, elastocapillary instabilities in soft filaments emerge that resemble the Plateau-Rayleigh (P–R) instabilities in liquids. The experimentally observed P–R instability of soft elastic filaments has been recently investigated via numerical and theoretical approaches. However, these contributions focus on the incompressible limit and preclude the nonlinear Poisson's ratio effects in materials, for example, compressible hydrogels with Poisson's ratios that can go as low as 0.1. Moreover, most of the research on the solid P–R instability elaborate on the onset, ignoring the post-bifurcation regime. Here we show that compressibility matters and the form of the assumed compressible strain energy density has a significant effect on the onset and the post-bifurcation behavior of elastic P–R instability. For example, the P–R instability can be entirely suppressed depending on the form of the free energy density and Poisson's ratio. To this end, we employ a robust and variational elastocapillary formulation and its computer implementation using surface-enriched isogeometric finite elements at finite strains. We use an arclength solver to illustrate both stable-unstable amplitude growth and bifurcation points in the entire equilibrium path. Stability maps are drawn with distinct stable-unstable regions over various shear modulus, surface tension, fiber radius, and applied stretch for cases ranging from quasi-compressible to fully compressible. The presented elastocapillary model proves to be useful in quantifying the surface and bulk energies in competition at finite strains and expected to help improve mechanical characterization of soft materials with at least one dimension that is on the orders of the elastocapillary lengthscale $l_{\text{solid}} \sim O(\text{nm} - \text{mm})$.

Keywords: Plateau Rayleigh instabilities, compressible elasticity, post bifurcation regime, surface tension

---

[*] Corresponding author.
Email addresses: `berkin@utexas.edu` (Berkin Dortdivanlioglu), `ajavili@bilkent.edu.tr` (Ali Javili)

1. Introduction

It is well-established that the external surface of a continuum body exhibits properties that differ from those of the encased bulk. The influence of the boundary on the material behavior, regardless of its physical nature, is more pronounced at smaller scales due to the increasing surface-to-volume ratio. Additionally, for very soft solids like gels, the surface energy is comparable to elastic bulk energy at macroscopic scales. The energetic competition between the bulk gel and its boundary leads to what is commonly referred to as the elastocapillary effect, which plays an important role in cavitation [1], soft composites behavior [2, 3], wetting on soft substrates [4–7], soft contact and adhesion [8, 9], fracture [10], capillary bending [11], and pattern formations in nature [12], to name few. Quantification of these surface forces for soft elastic materials is an active research field [13, 14]. A seminal study in this area is the work of Mora, *et al.* [15] that reports experimental evidence of capillary-induced bead formations at thin, gel filaments due to elastic Plateau–Rayleigh (P–R) instabilities. The main objective of this manuscript is to investigate the elastic P–R instabilities in soft solids thereby pre- and post-bifurcation regimes are carefully examined from fully compressible to quasi-incompressible material behaviors. The main ingredients of the work presented here are (i) elastocapillary theory and (ii) elastic Plateau–Rayleigh instability. A brief review of these topics is now given.

1.1. State of the art review of elastocapillary theory

The elastocapillary theory and surface modeling of continua can be traced back to the pioneering works of Laplace, Young and Gibbs. Following Gibbsian thermodynamics and a seminal work of Scriven [16], Gurtin and Murdoch [17] developed a phenomenological *surface elasticity model* that has been widely adopted for applications in nanomaterials, see [18–22] among others. The surface elasticity theory assumes that a surface possesses its own tensorial stress which derives from the surface constitutive laws. That is, surface stresses are acquired as energetically conjugated quantities to surface strains since the surface is endowed with its own thermodynamic structure. As a result, capillary effects are intrinsically accounted for in the surface elasticity theory. Surface effects introduce a physical length-scale that is otherwise lacking in classical continuum mechanics since the surface-to-volume ratio is proportional to the inverse of the domain size. Numerous analytical [18–21] and computational [23–25] studies have demonstrated that the size-dependent material response due to surface elasticity is physically meaningful and is also in agreement with atomistic simulations [26–29]. From a computational perspective, the finite element modeling of surface tension for *fluids* was carried by Saksono and Perić [30, 31] for quasi-static and dynamic problems, see also [32]. This formulation is suitable for fluids in that the surface tension is accounted for but the surface elasticity is absent. To address this issue, Yvonnet, *et al.* [23] introduced surface elasticity into the finite element method for *solids* though at small strains in two dimensions only. Javili and Steinmann [33, 34] developed a finite element framework for continua with boundary energies that accounted for surface elasticity as well as surface tension for two-dimensional [33] and three-dimensional [34] solids at *finite deformations*. Henann and Bertoldi [35] employed this framework and established a numerical procedure appropriate for modeling elastocapillary phenomena using the commercial finite element (FE) package Abaqus and studied a variety of problems, see also [36]. A similar approach was adopted by Mora, *et al.* [37] and an ad-hoc numerical code using the FEniCS finite element library has been provided. He and Park [38] presented a computational methodology to capture elastocapillary, essentially equivalent to the classical Young–Laplace model, that could be readily incorporated to commercial FE packages such as ANSYS and COMSOL, see also [39].

The surface elasticity theory has experienced a prolific growth in the past two decades [40] and the aforementioned contributions are only given as a few examples among many others. This resurgence of interest in the mechanics of solid surfaces can be largely attributed to the increasing number of applications involving nanoscale structures and soft solids such as gels. From a theoretical standpoint also various extensions of the surface elasticity theory have also been proposed. For example, Steigmann and Ogden [41] extended the theory to account for the flexural resistance of the surface against the changes of its curvature. Another important extension is the interface elasticity theory [42, 43] leading to thermo-mechanical interfaces [22, 44] and general interface models [45–47]. Also, surface viscoelasticity has drawn a considerable attention and recently studied in [48–52].

Here, we employ a variational elastocapillary theory at finite deformations in that the Young–Laplace equation does not explicitly appear in the governing equations. More precisely, unlike the commonly accepted approach that introduces the surface tension in an ad-hoc manner via an external force on the surface, we capture the surface tension via its energy representation as a constant energy density per surface area in the spatial configuration. This subtle point allows for a more elegant approach to P–R instability wherein only internal energy densities enter into the picture. This approach is particularly useful from a computational perspective in that it furnishes an appropriate framework for the problem at hand and the nonlinear stability analysis for the P–R problem.

1.2. State of the art review of solid Plateau–Rayleigh instability

Capillary forces can trigger P–R instability in both fluids and soft solids. In *fluids*, surface tension overwhelms cylindrical liquid columns and causes surface undulations with a well-defined wavelength along its length, creating a periodic pattern. Eventually, the resulting waves in the liquid column grow and break up into regularly spaced spherical droplets [53]. From an energetic consideration, this column-to-droplet transition is due to the vanishing shear resistance of the bulk fluid, which facilitates a final configuration with minimal surface area attained under constant volume, i.e. a sphere formation [54]. In the case of *soft solids*, the bulk elasticity will resist the surface tension, playing a fundamental role in solid P–R instability characteristics [55, 56]. For example, Mora, *et al.* (2010)

have given the first experimental evidence of solid P–R instability, demonstrating that agar gel fibers form cylindrical bead patterns (contrary to spherical beads in fluid jets) without complete breakup [15]. The energetic competition between bulk elastic deformations and capillary action determines the equilibrium pattern. This competition can be quantified through a characteristic length scale, conceptually $\ell = \gamma/\mu$, where γ is the surface tension constant and μ is the bulk shear modulus. For example, in stiff materials ($\mu \sim$ MPa), the dimension of length ℓ ranges in the order of nanometers; consequently the bulk elasticity overwhelms the material behavior at macroscopic scales. On the other hand, for soft solids ($\mu \sim$ Pa), surface tension can dominate the overall deformations in balance with the bulk elasticity at relatively larger length scales, i.e., $\ell \sim$ mm, for example, see [37, 57].

The solid P–R instability has been investigated using numerical and theoretical approaches. Mora, *et al.* (2010) performed a linear stability analysis for a slender elastic fiber, successfully predicting the bifurcation-onset strain in close match their experiments [15]. Performing a weakly nonlinear stability analysis using hyperelastic solid models, Taffetani and Ciarletta (2015) concluded that two dimensionless parameters (i) the axial stretch and (ii) the elastocapillary ratio $\ell/R_\circ$ control the onset and the amplitude growth, where $R_\circ$ is the radius of the soft fiber [58, 59]. Further investigations, including recent nonlinear finite element simulations accounting for capillary forces, are carried out to elucidate the effect of electric field [39], active surface contraction [60], growth and swelling [61, 62], and hollow tube geometry [35, 63–65] in P–R instability. Such approaches, however, have failed to quantify the selection of wave number (or pattern) at the bifurcation-onset. In contrast to the experimental findings, the existing methods employing quasi-static stability analysis predict infinite-wavelength for the pattern, suggesting global deformations rather than periodic waves [66, 67]. Recently, Pandey, *et al.* (2020) performed a dynamic analysis using hyperelastic solids, indicating that the pattern selection, i.e., the critical wavelength of cylinder-like formations, is due to a dynamical process, similar to the selection of bead size in fluid P–R instabilities [68].

In the post-instability regime, fully nonlinear FE analysis predicts that solid column deforms into cylinders with two distinct radii connected by a transition region with a finite width [69], in a close analogy to phase-separation-like behavior of inflating hyperelastic, cylindrical balloons [70, 71]. Surprisingly, both cylinder radii remain constant under increasing end stretches over several hundred percent strains [69]. Another fundamental difference of P–R instabilities in fluids and solids is that, while fluid beading develops as a supercritical (continuous) bifurcation, its solid counterpart, in general, demonstrates a subcritical (discontinuous) behavior [59, 66, 67]. Recent work have derived efficient, one-dimensional models closely matching onset and amplitude evolution predicted by nonlinear finite element simulations and weakly nonlinear analysis, even at localized deformations far away from the onset [72]. However, most studies in the field of solid P–R problem have so far only focused on truly incompressible elastic cylinders and, in particular, on the onset of the instability. Very recently, Tamim and Bostwick (2021) performed stability analysis assuming small strains for a compressible viscoelastic material concluding that, while viscous effects stabilize the P–R instability, compressibility destabilizes as it promotes an earlier bifurcation-onset [73].

1.3. Key features and novelties

Compared to earlier works on the topic, to the best of our knowledge, there are several important areas and conclusions where this study makes an original contribution to. In summary, the key features and contributions of the manuscript are:

- to study Plateau–Rayleigh instabilities of *compressible soft solids*. Thereby, we illustrate that compressibility matters and, unlike the incompressibility limit, the form of the neo-Hookean free energy density matters when the compressibility is accounted for,
- to show that - unlike the incompressibility limit - Plateau–Rayleigh instabilities can be avoided altogether for compressible soft solids depending on the amount of stretch, Poisson's ratio and the form of the free energy density,
- to present the full equilibrium path, including stable-unstable states, of solid Plateau–Rayleigh instabilities using an arc-length method, for the first time.

1.4. Notation and definitions

Direct notation is adopted throughout. Occasional use is made of index notation, the summation convention for repeated indices being implied. The scalar product of two vectors $\boldsymbol{a}$ and $\boldsymbol{b}$ is denoted $\boldsymbol{a} \cdot \boldsymbol{b} = [\boldsymbol{a}]_i[\boldsymbol{b}]_i$. The scalar product of two second-order tensors $\boldsymbol{A}$ and $\boldsymbol{B}$ is denoted $\boldsymbol{A} : \boldsymbol{B} = [\boldsymbol{A}]_{ij}[\boldsymbol{B}]_{ij}$. The composition of two second-order tensors $\boldsymbol{A}$ and $\boldsymbol{B}$, denoted $\boldsymbol{A} \cdot \boldsymbol{B}$, is a second-order tensor with components $[\boldsymbol{A} \cdot \boldsymbol{B}]_{ij} = [\boldsymbol{A}]_{is}[\boldsymbol{B}]_{sj}$. The surface quantities are distinguished from their bulk counterparts by an accent on top. That is, quantities or operators $\{\hat{\bullet}\}$ are the surface counterparts of the bulk quantity or operator $\{\bullet\}$, respectively, unless specified otherwise. The fourth-order identity tensor is denoted as $\mathbb{I}$. Similarly, other fourth-order constitutive tensors are also written with the same font, such as $\mathbb{A}$ for the fourth-order tangent tensor. The tensor product of two second-order tensors $\boldsymbol{A}$ and $\boldsymbol{B}$ is a fourth-order tensor $\mathbb{D} = \boldsymbol{A} \otimes \boldsymbol{B}$ with $[\mathbb{D}]_{ijkl} = [\boldsymbol{A}]_{ij}\,[\boldsymbol{B}]_{kl}$. The two non-standard tensor products of two second-order tensors $\boldsymbol{A}$ and $\boldsymbol{B}$ are the fourth-order tensors $[\boldsymbol{A} \overline{\otimes} \boldsymbol{B}]_{ijkl} = A_{ik}\,B_{jl}$ and $[\boldsymbol{A} \underline{\otimes} \boldsymbol{B}]_{ijkl} = A_{il}\,B_{jk}$.

1.5. Organization of the manuscript

This manuscript is organized as follows. Section 2 lays the theoretical foundation for the study. First, the kinematics of the problem is formulated and the key concepts of differential geometry required to describe the boundary motion are briefly reviewed in Section 2.1 followed by a generic three-dimensional framework suitable for a surface tension theory that is concisely introduced in Section 2.2. The connection to Plateau–Rayleigh instabilities is established via an eigenvalue analysis in Section 2.3. Thanks to the variational approach, the governing equations naturally emerge in their weak forms that are immediately suitable for computational implementation elaborated in Section 2.4. In particular, isogeometric analysis [74] is utilized since it inherently and elegantly accounts for the boundary. The developed framework and its utility to capture P–R instabilities is elucidated via a series of numerical examples in Section 3. The numerical examples are devised such that both computational and physical aspects of the problem are covered. We thoroughly investigate the onset of instabilities as well as post-bifurcation behavior of compressible soft solids. Section 4 concludes this work and provides an outlook for future work.

2. Theory

The objective of this section is to establish the governing equations of elasticity at finite deformations accounting for surface tension, wherein the boundary of a body is endowed with its own free energy density. We provide a formulation such that the governing equations will be established in their integral forms immediately suited for computational implementation. Another feature of the current approach is that the kinematic measures are formulated in a unified and consistent manner fitting to IGA.

2.1. Preliminaries

Consider the deformation of a continuum body, as illustrated in Fig. 1 that occupies the material configuration $\mathscr{B}_0 \subset \mathbb{R}^3$ at time $t = 0$ that is mapped to the spatial configuration $\mathscr{B}_t \subset \mathbb{R}^3$ at any time $t > 0$ via the nonlinear deformation map $\boldsymbol{\varphi}$ as

$$\boldsymbol{x} = \boldsymbol{\varphi}(\boldsymbol{X}, t) \ : \ \mathscr{B}_0 \times \mathbb{R}_+ \to \mathscr{B}_t \qquad \text{and} \qquad \hat{\boldsymbol{x}} = \boldsymbol{\varphi}(\hat{\boldsymbol{X}}, t) \ : \ \mathscr{S}_0 \times \mathbb{R}_+ \to \mathscr{S}_t \,, \tag{1}$$

with $\boldsymbol{X}$ and $\boldsymbol{x}$ identifying points in the material and spatial configurations, respectively. According to our convention, the surface quantities are denoted as $\{\hat{\bullet}\}$. That is, the placement of particles on the surface are labeled $\hat{\boldsymbol{X}}$ and $\hat{\boldsymbol{x}}$ in the material and spatial configurations, respectively, such that $\hat{\boldsymbol{X}} = \boldsymbol{X}|_{\mathscr{S}_0}$ and $\hat{\boldsymbol{x}} = \boldsymbol{x}|_{\mathscr{S}_t}$, where $\mathscr{S}_0 := \partial\mathscr{B}_0$ and $\mathscr{S}_t := \partial\mathscr{B}_t$. The boundary is material in the sense that the boundary is convected with the domain and remains perfectly bonded to the bulk throughout deformations. The deformation gradient in the bulk, denoted $\boldsymbol{F} := \mathrm{Grad}\boldsymbol{\varphi}$, is a linear deformation map that relates an infinitesimal line element $\mathrm{d}\boldsymbol{X} \in T\mathscr{B}_0$ to its spatial counterpart $\mathrm{d}\boldsymbol{x} \in T\mathscr{B}_t$ via the relation $\mathrm{d}\boldsymbol{x} = \boldsymbol{F}\cdot\mathrm{d}\boldsymbol{X}$ and therefore $\boldsymbol{F} = \boldsymbol{g}_i \otimes \boldsymbol{G}^i$ with its inverse defined as $\boldsymbol{f} := \boldsymbol{G}_i \otimes \boldsymbol{g}^i$ where $\boldsymbol{G}^i$ are the contravariant basis vectors in the

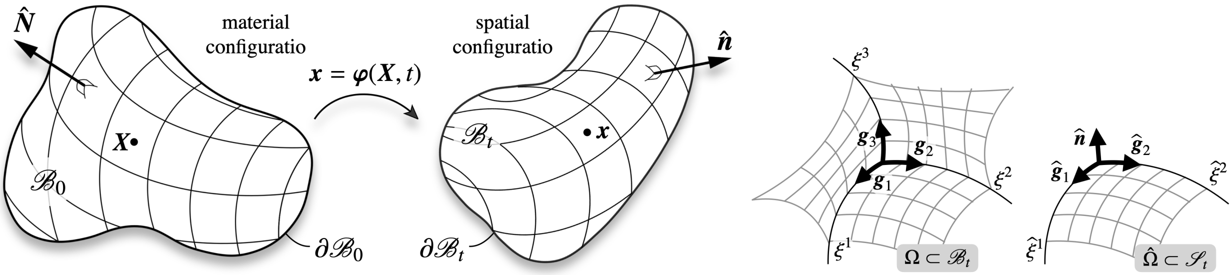

Figure 1: Finite deformation of a continuum body (left). The continuum body that occupies the material configuration $\mathscr{B}_0 \subset \mathbb{R}^3$ at time $t = 0$ is mapped to the spatial configuration $\mathscr{B}_t \subset \mathbb{R}^3$ via the nonlinear deformation map $\boldsymbol{\varphi}$. The boundary points are convected via the same deformation map $\boldsymbol{\varphi}$ as the bulk. Graphical illustration of the covariant basis vectors on $\mathscr{B}_t$ and $\mathscr{S}_t$ (right). The domains Ω and $\hat{\Omega}$ indicate an arbitrary cutout subdomain of $\mathscr{B}_t$ and $\mathscr{S}_t$, respectively.

material configuration. The contravariant vectors $\boldsymbol{G}^i$ and $\boldsymbol{g}^i$ form a dual basis to the covariant (natural) basis $\boldsymbol{G}_i$ and $\boldsymbol{g}_i$, in the material and spatial configurations, respectively. That is $\boldsymbol{G}_i := \partial\boldsymbol{X}/\partial\xi^i$ and $\boldsymbol{g}_i := \partial\boldsymbol{x}/\partial\xi^i$ such that $\boldsymbol{G}_i \cdot \boldsymbol{G}^j = \delta_i^j$ and $\boldsymbol{g}_i \cdot \boldsymbol{g}^j = \delta_i^j$, where δ_i^j is the Kronecker delta. The properties $\boldsymbol{F} \cdot \boldsymbol{f} = \boldsymbol{i}$ and $\boldsymbol{f} \cdot \boldsymbol{F} = \boldsymbol{I}$ hold with $\boldsymbol{I}$ and $\boldsymbol{i}$ being the (mixed-variant) bulk identity tensors in the material and spatial configurations, respectively, as $\boldsymbol{I} := \boldsymbol{G}_i \otimes \boldsymbol{G}^i$ and $\boldsymbol{i} := \boldsymbol{g}_i \otimes \boldsymbol{g}^i$. See Fig. 1 (right) for a graphical illustration of the covariant basis vectors in the bulk and on the boundary. The ratio of the volume element in the spatial configuration $\mathrm{d}v$ over its counterpart in the material configuration $\mathrm{d}V$ is the Jacobian $J := \mathrm{d}v/\mathrm{d}V = \mathrm{Det}\boldsymbol{F}$.

The surface $\mathscr{S}_0$ or $\mathscr{S}_t$ in the material or spatial configurations, respectively, is a two-dimensional manifold in the three-dimensional space $\mathbb{R}^3$ that can be parametrized in terms of two surface (curvilinear) coordinates $\hat{\xi}^\alpha$. The corresponding tangent vectors to the surface coordinate lines $\hat{\xi}^\alpha$ are the covariant (natural) surface basis vectors $\hat{\boldsymbol{G}}_\alpha$ and the surface deformation gradient rea d$\hat{\boldsymbol{F}} := \hat{\boldsymbol{g}}_\alpha \otimes \hat{\boldsymbol{G}}^\alpha$ with its inverse $\hat{\boldsymbol{f}} := \hat{\boldsymbol{G}}_\alpha \otimes \hat{\boldsymbol{g}}^\alpha$ possessing the properties $\hat{\boldsymbol{F}} \cdot \hat{\boldsymbol{f}} = \hat{\boldsymbol{i}}$ and $\hat{\boldsymbol{f}} \cdot \hat{\boldsymbol{F}} = \hat{\boldsymbol{I}}$ with $\hat{\boldsymbol{I}}$ and $\hat{\boldsymbol{i}}$ being the surface identity tensors in the material and spatial configurations, respectively. The surface contravariant vectors $\hat{\boldsymbol{G}}^\alpha$ and $\hat{\boldsymbol{g}}^\alpha$ form a dual basis to the covariant (natural) basis $\hat{\boldsymbol{G}}_\alpha$ and $\hat{\boldsymbol{g}}_\alpha$, in the material and spatial configurations, respectively. That is $\hat{\boldsymbol{G}}^\alpha := \partial\hat{\xi}^\alpha/\partial\hat{\boldsymbol{X}}$ and $\hat{\boldsymbol{g}}^\alpha := \partial\hat{\xi}^\alpha/\partial\hat{\boldsymbol{x}}$ such that $\hat{\boldsymbol{G}}_\alpha \cdot \hat{\boldsymbol{G}}^\beta = \delta_\alpha^\beta$ and $\hat{\boldsymbol{g}}_\alpha \cdot \hat{\boldsymbol{g}}^\beta = \delta_\alpha^\beta$. Similarly to the bulk, we define the surface deformation gradient $\hat{\boldsymbol{F}}$ as the linear map between the infinitesimal line element $\mathrm{d}\hat{\boldsymbol{X}} \in T\mathscr{S}_0$ and $\mathrm{d}\hat{\boldsymbol{x}} \in T\mathscr{S}_t$ with $\mathrm{d}\hat{\boldsymbol{x}} = \hat{\boldsymbol{F}} \cdot \mathrm{d}\hat{\boldsymbol{X}}$. In contrast to the bulk, the surface identities $\hat{\boldsymbol{I}}$ and $\hat{\boldsymbol{i}}$ are not equal since $\hat{\boldsymbol{I}} := \hat{\boldsymbol{G}}_\alpha \otimes \hat{\boldsymbol{G}}^\alpha = \boldsymbol{I} - \hat{\boldsymbol{N}} \otimes \hat{\boldsymbol{N}}$ and $\hat{\boldsymbol{i}} := \hat{\boldsymbol{g}}_\alpha \otimes \hat{\boldsymbol{g}}^\alpha = \boldsymbol{i} - \hat{\boldsymbol{n}} \otimes \hat{\boldsymbol{n}}$ where $\hat{\boldsymbol{N}}$ and $\hat{\boldsymbol{n}}$ denote the unit vector orthogonal to the surface in the material and spatial configurations, respectively. The ratios of area elements in the spatial over the material configuration is defined by $\hat{J}$, as $\hat{J} := \mathrm{d}a/\mathrm{d}A$ which is the surface determinant of $\hat{\boldsymbol{F}}$ though, in contrast to the bulk, $\hat{\boldsymbol{F}}$ is rank-deficient and thus, its determinant is non-standard.

2.2. *Generic framework accounting for elastocapillary*

The objective of this section is to derive the governing equations of a continuum body accounting for surface tension in a variationally consistent framework such that (i) it immediately allows for an elegant axi-symmetric formulation, devoid of external contributions and (ii) it intrinsically results in governing equations in their (weak) integral form directly suitable for computational implementation in that Young–Laplace equation does not explicitly appear throughout the manuscript. This advantage is significant since the surface curvature and surface divergence operator remain embedded in the framework without emerging in the derivations. In addition, the variational approach here paves the way to extending the proposed framework to higher-gradient continua e.g. accounting for the flexural resistance of the surface. In order to obtain the governing equations, the total energy functional is minimized. The total energy functional Ψ^{tot} consists of the internal and external contributions denoted Ψ^{int} and Ψ^{ext}, respectively. To minimize Ψ^{tot}, its first variation is set to zero as

$$\Psi^{\text{tot}} = \Psi^{\text{int}} + \Psi^{\text{ext}} \qquad , \qquad \text{equilibrium} \equiv \delta\Psi^{\text{tot}} \doteq 0 \qquad \Rightarrow \qquad \delta\Psi^{\text{tot}} = \delta\Psi^{\text{int}} + \delta\Psi^{\text{ext}} \doteq 0\,. \tag{2}$$

The (incremental) external energy here Ψ^{ext} is essentially minus (incremental) working. That is

$$\delta\Psi^{\text{ext}} = -\delta\mathcal{W} \qquad \text{with} \qquad \delta\mathcal{W} = \int_{\mathscr{B}_0} \boldsymbol{b}_0 \cdot \delta\boldsymbol{\varphi}\,\mathrm{d}V + \int_{\partial\mathscr{B}_0} \boldsymbol{t}_0 \cdot \delta\boldsymbol{\varphi}\,\mathrm{d}A\,, \tag{3}$$

in which $\mathcal{W}$ denotes working. Also, $\boldsymbol{b}_0$ and $\boldsymbol{t}_0$ are the external body force density and surface force density in the material configuration, respectively. The arbitrary variation of motion, denoted as $\delta\boldsymbol{\varphi}$, is a vector-valued test function $\delta\boldsymbol{\varphi} \in \mathscr{H}^1_0(\mathscr{B}_0)$ that is vanishing where Dirichlet-type boundary conditions are imposed. This subtle detail plays a crucial role in the current contribution in that it makes $\delta\Psi^{\text{ext}}$ identically vanish. More specifically, for the problem of interest here, shown in Fig. 2, the external body forces are zero and therefore the first integral in Eq. (3) vanishes identically. Thus, the working $\mathcal{W}$ only depends on the external traction $\boldsymbol{t}_0$. Nonetheless, the second integral in Eq. (3) vanishes too, since (i) $\delta\boldsymbol{\varphi}$ is zero where displacements are prescribed on the two ends of the domain and (ii) $\boldsymbol{t}_0$ is zero everywhere that a Neumann-type boundary condition is imposed. The latter immediately follows from the fact that here, the surface tension is not treated on ad-hoc basis via an externally prescribed traction on the surface, but instead, it is captured within the internal energy density of the surface. Henceforth, we impose $\delta\Psi^{\text{ext}} = 0$ throughout the derivations, and therefore we focus on the internal energy variation $\delta\Psi^{\text{int}}$ only. The internal energy Ψ^{int} is composed of bulk and surface contributions. Let ψ denote the bulk free energy density per volume in the material configuration and $\hat{\psi}$ denote the surface free energy density per area in the spatial configuration. Therefore, Ψ^{int} reads

$$\Psi^{\text{int}} = \int_{\mathscr{B}_0} \psi \, \mathrm{d}V + \int_{\partial\mathscr{B}_0} \hat{\psi} \, \mathrm{d}A \, . \tag{4}$$

Therefore, from a variational perspective, equilibrium for the current problem reduces to

$$\delta\Psi^{\text{int}} = \int_{\mathscr{B}_0} \delta\psi \, \mathrm{d}V + \int_{\partial\mathscr{B}_0} \delta\hat{\psi} \, \mathrm{d}A \doteq 0 \quad \Rightarrow \quad \int_{\mathscr{B}_0} \frac{\partial\psi}{\partial\boldsymbol{\varphi}} \cdot \delta\boldsymbol{\varphi} \, \mathrm{d}V + \int_{\partial\mathscr{B}_0} \frac{\partial\hat{\psi}}{\partial\boldsymbol{\varphi}} \cdot \delta\boldsymbol{\varphi} \, \mathrm{d}A \doteq 0 \quad \forall \delta\boldsymbol{\varphi} \in \mathscr{H}^1_0(\mathscr{B}_0) \, . \tag{5}$$

The arbitrary motion variations $\delta\boldsymbol{\varphi}$ in the context of IGA can be expressed in their discretized form as $\delta\boldsymbol{\varphi} = N^i \, \delta\boldsymbol{\varphi}^i$, with N^i being the (NURBS) shape function associated with the control point i. Due to the arbitrariness of $\delta\boldsymbol{\varphi}^i$, Eq. (5) can be *formally* expressed as $\boldsymbol{R}^I \cdot \delta\boldsymbol{\varphi}^I \doteq 0$ for all arbitrary $\delta\boldsymbol{\varphi}^I$ which immediately implies $\boldsymbol{R}^I \doteq \boldsymbol{0}$ with $\boldsymbol{R}^I = \mathbf{A}\, \boldsymbol{R}^i$. Here $\boldsymbol{R}^i$ the point-wise residual at point i associated with its global number I and $\mathbf{A}$ is the assembly operator. That is, we seek for the solutions of

$$\boldsymbol{R}^I \doteq \boldsymbol{0} \qquad \text{with} \qquad \boldsymbol{R}^I := \int_{\mathscr{B}_0} \frac{\partial\psi}{\partial\boldsymbol{\varphi}^i} \, \mathrm{d}V + \int_{\partial\mathscr{B}_0} \frac{\partial\hat{\psi}}{\partial\boldsymbol{\varphi}^i} \, \mathrm{d}A \, . \tag{6}$$

The residual vector is obviously composed of the residuals in the bulk and the residuals on the surface. Equation (6) is the point of departure for the remaining discussions. Note that Eq. (6) is essentially a nonlinear system of equations composed of DOFs relations, with DOFs being the number of degrees of freedom. For nonlinear problems at large deformations, the deformation is computed incrementally. To solve the nonlinear system of equations (6), at each increment, an iterative Newton–Raphson scheme is utilized. In doing so, the global residual $\boldsymbol{R}$ is set to zero at (the end of) each increment. Therefore, the consistent linearization of the resulting system of equations at any iteration k, reads

$$\boldsymbol{R}^I(\boldsymbol{\varphi}_{k+1}) \doteq \boldsymbol{0} \qquad \text{and} \qquad \boldsymbol{R}^I(\boldsymbol{\varphi}_{k+1}) = \boldsymbol{R}^I(\boldsymbol{\varphi}_k) + \boldsymbol{K}^{IJ}\big|_k \cdot \Delta\boldsymbol{\varphi}^J_k \doteq \boldsymbol{0} \qquad \text{with} \qquad \boldsymbol{K}^{IJ} = \frac{\partial \boldsymbol{R}^I}{\partial\boldsymbol{\varphi}^J} \, , \tag{7}$$

where $\boldsymbol{K}^{IJ}$ is the tangent stiffness at any $\boldsymbol{\varphi}_k$. Then the global deformation is updated at each iteration according to $\boldsymbol{\varphi}_{k+1} = \boldsymbol{\varphi}_k + \Delta\boldsymbol{\varphi}_k$ until the norm of the residual vector reaches zero, numerically speaking.

2.3. Plateau–Rayleigh instabilities

The procedure to capture P–R instabilities in the manuscript relies on an eigenvalues analysis. In doing so, at each increment an eigenvalue analysis is carried out on the stiffness $\boldsymbol{K}$. Plateau–Rayleigh instabilities occur as soon as the stiffness matrix loses its positive-definiteness, which is equivalently captured when at least one eigenvalue of

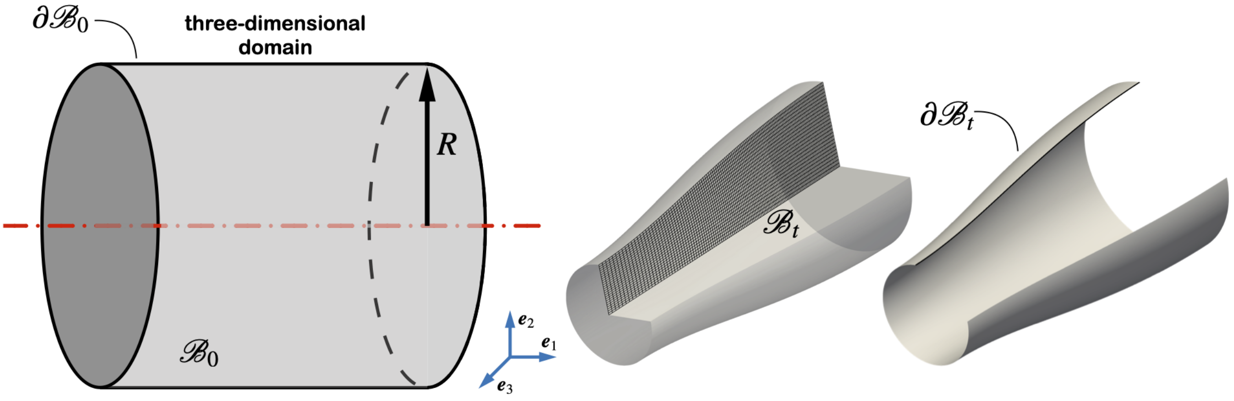

Figure 2: Geometry of the domain in the material (left) and spatial (right) configurations.

$\boldsymbol{K}$ becomes smaller or equal to zero. The eigenvector corresponding to the negative eigenvalue shows the associated instability mode. Note that on the onset of P–R instability, we expect at least one eigenvalue to become negative but we observe multiple negative eigenvalues as we progress further in the unstable regime. Figure 3 clearly shows how the onset of P–R instability can be identified from the eigenvalues of the stiffness $\boldsymbol{K}$, for any prescribed stretch on the domain. For any prescribed stretch λ, the critical value for (dimensionless) $\Gamma := \gamma/\mu R$ corresponds to the first instance of observing an eigenvalue smaller or equal to zero, with γ and μ being the surface tension and shear modulus, respectively. The radius of the domain in the reference configuration is denoted R. Each point on the graph shows the number of negative eigenvalues of $\boldsymbol{K}$ obtained via simulations corresponding to nearly incompressible neo-Hookean hyperelastic solids, commonly studied in the literature on the subject. In this particular example, and for the sake of clarity, we preclude post-bifurcation behavior by suppressing the perturbations. That is, we carry out a purely perturbation-free eigenvalue analysis so that the computations can continue even in the unstable regime. Throughout the stable regime, $\boldsymbol{K}$ remains symmetric and positive-definite and thus, all the eigenvalues of $\boldsymbol{K}$ are positive.

Having established the final format for the residual and the tangent stiffness, the last step is to set the free energy densities ψ in the bulk and $\hat{\psi}$ on the surface. For the bulk free energy density ψ, however, various options are available in literature. In particular, since this manuscript aims to study the influence of *compressibility* on P–R instability, we investigate two options to portray a more complete picture. Two commonly used free energy densities for compressible hyperelastic materials are

$$\begin{aligned}
&\text{Quadratic} && : \quad \psi(\boldsymbol{F}) = \frac{1}{2}\,\mu\,[\,\boldsymbol{F}:\boldsymbol{F} - 3 - 2\log J\,] + \frac{1}{2}\,\lambda\,[\,\tfrac{1}{2}[J^2 - 1] - \log J\,]\,,\\
&\text{Logarithmic} && : \quad \psi(\boldsymbol{F}) = \frac{1}{2}\,\mu\,[\,\boldsymbol{F}:\boldsymbol{F} - 3 - 2\log J\,] + \frac{1}{2}\,\lambda\,\log^2 J\,,
\end{aligned} \tag{8}$$

with the first and second Lamé parameters being λ and μ, respectively. Obviously, the difference amongst the energy

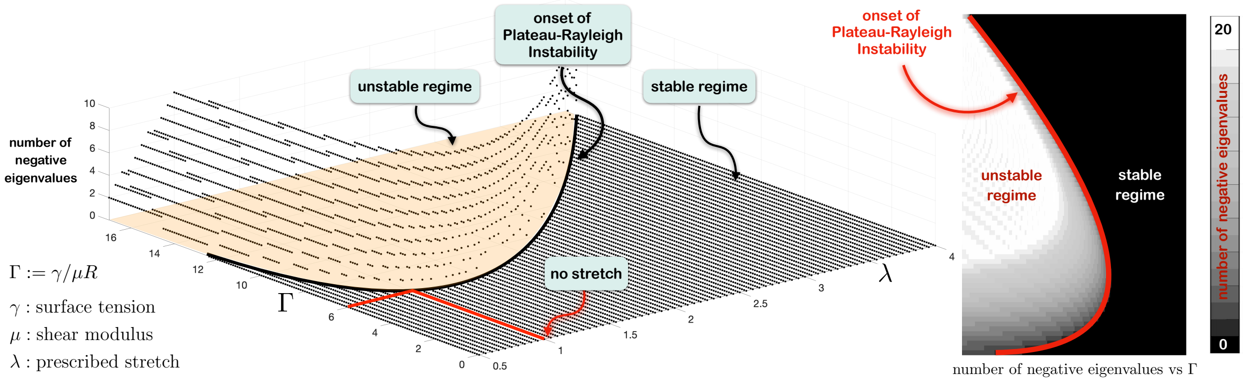

Figure 3: Relationship between the eigenvalues of the stiffness $\boldsymbol{K}$ and the onset of P–R instability. For any prescribed stretch λ, the critical value for $\Gamma := \gamma/\mu R$ corresponds to the first instance of observing an eigenvalue smaller or equal to zero. Note that in this particular example, and for the sake of clarity, we preclude post-bifurcation behavior via suppressing the perturbations. The simulations correspond to nearly incompressible neo-Hookean hyperelastic solids, commonly studied in the literature on the subject.

densities is the penalty term in terms of J that resists to the volume change, and both energies render identical results at the incompressibility limit. Figure 4 illustrates the behavior of the second term of both options (8). Table 1 and Table 2 gather the free energy densities of interest together with their associated Piola stress $\boldsymbol{P}$ and tangent $\mathbb{A}$, wherein the fourth-order tensors $\mathbb{H} := \boldsymbol{I} \overline{\otimes} \boldsymbol{I}$, $\mathbb{G} := \boldsymbol{F}^{\text{-t}} \underline{\otimes} \boldsymbol{F}^{-1}$ and $\mathbb{E} := \boldsymbol{F}^{\text{-t}} \otimes \boldsymbol{F}^{\text{-t}}$ are defined to obtain more elegant tangents.

Table 1: The quadratic free energy density $(8)_1$ together with its corresponding first and second derivatives with respect to $\boldsymbol{F}$.

$$
\begin{aligned}
\psi(\boldsymbol{F}) &= \frac{1}{2}\mu\,[\,\boldsymbol{F}:\boldsymbol{F} - 3 - 2\log J\,] + \frac{1}{2}\lambda\,[\,\tfrac{1}{2}[J^2-1] - \log J\,]\,,\\
\boldsymbol{P} := \frac{\partial\psi}{\partial\boldsymbol{F}} &= \mu\,[\boldsymbol{F} - \boldsymbol{F}^{\text{-t}}] + \frac{1}{2}\lambda\,[J^2-1]\,\boldsymbol{F}^{\text{-t}}\,,\\
\mathbb{A} := \frac{\partial\boldsymbol{P}}{\partial\boldsymbol{F}} &= \mu\,[\mathbb{H} + \mathbb{G}] - \frac{1}{2}\lambda\,[J^2-1]\,\mathbb{G} + \lambda\,J^2\,\mathbb{E}\,.
\end{aligned}
$$

While one can study various free energy densities in the bulk to investigate the influence of compressibility, the surface free energy density is devoid of elasticity contributions and requires only to represent a constant surface tension. As such, and since the surface free energy density per unit area in the current configuration is constant and coincides with the surface tension $\hat{\gamma}$, the surface free energy density simply reads

$$
\hat{\psi} = \hat{\gamma}\,\hat{J} \qquad \text{with} \qquad \hat{\gamma} : \text{surface tension} \qquad \text{and} \qquad \hat{J} := \widehat{\mathrm{Det}}\hat{\boldsymbol{F}} = \mathrm{d}a/\mathrm{d}A\,. \tag{9}
$$

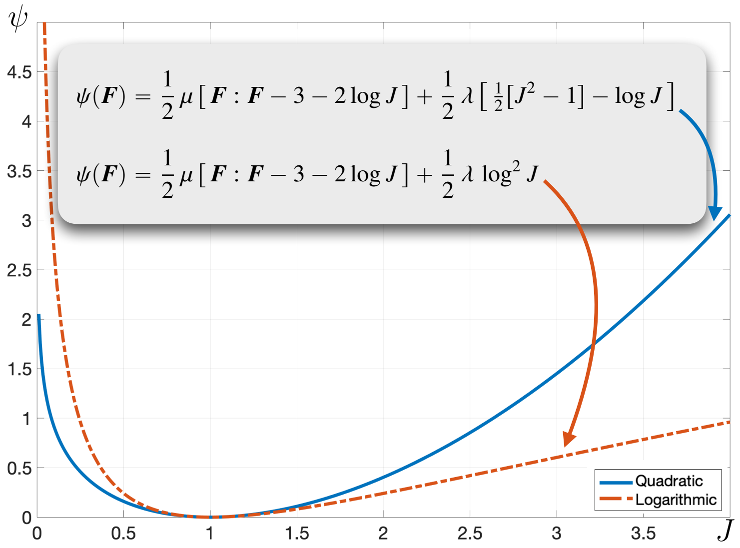

Figure 4: Comparing the penalty term of free energy densities (8) To have a meaningful comparison, $\mu = 0$ is assumed for all the energies.

Table 2: The logarithmic free energy density $(8)_2$ together with its corresponding first and second derivatives with respect to $\boldsymbol{F}$.

$$
\begin{aligned}
\psi(\boldsymbol{F}) &= \frac{1}{2}\mu\,[\,\boldsymbol{F}:\boldsymbol{F} - 3 - 2\log J\,] + \frac{1}{2}\lambda\,\log^2 J\,,\\
\boldsymbol{P} := \frac{\partial\psi}{\partial\boldsymbol{F}} &= \mu\,[\boldsymbol{F} - \boldsymbol{F}^{\text{-t}}] + \lambda\,\log J\,\boldsymbol{F}^{\text{-t}}\,,\\
\mathbb{A} := \frac{\partial\boldsymbol{P}}{\partial\boldsymbol{F}} &= \mu\,[\mathbb{H} + \mathbb{G}] - \lambda\,\log J\,\mathbb{G} + \lambda\,\mathbb{E}\,.
\end{aligned}
$$

The corresponding surface Piola stress $\hat{\boldsymbol{P}}$ and its tangent $\hat{\mathbb{A}}$ read

$$
\hat{\psi} = \hat{\gamma}\,\hat{J} \qquad \Rightarrow \qquad \hat{\boldsymbol{P}} := \frac{\partial\hat{\psi}}{\partial\hat{\boldsymbol{F}}} = \hat{\gamma}\,\hat{J}\,\hat{\boldsymbol{F}}^{\text{-t}} \qquad \Rightarrow \qquad \hat{\mathbb{A}} := \frac{\partial\hat{\boldsymbol{P}}}{\partial\hat{\boldsymbol{F}}} = \hat{\gamma}\,\hat{J}\,[\hat{\mathbb{E}} - \hat{\mathbb{G}}]\,, \tag{10}
$$

with $\hat{\mathbb{G}} := \hat{\boldsymbol{F}}^{\text{-t}} \underline{\otimes} \hat{\boldsymbol{F}}^{\text{-1}} - [\hat{\boldsymbol{n}} \otimes \hat{\boldsymbol{n}}] \overline{\otimes} [\hat{\boldsymbol{F}}^{\text{-1}} \cdot \hat{\boldsymbol{F}}^{\text{-t}}]$ and $\hat{\mathbb{E}} := \hat{\boldsymbol{F}}^{\text{-t}} \otimes \hat{\boldsymbol{F}}^{\text{-t}}$.

2.4. Isogeometric formulation and discretization

In this section, we provide a brief overview of b-splines, which are standard for smooth representation of geometries in computer aided design and computer graphics software, and their implementation for bulk-boundary coupled axisymmetric discretization using isogemetric finite element analysis (IGA). To define i^{th} b-spline function $N_{i,p}$ of polynomial degree p, consider a non-decreasing set of real numbers in the knot vector $\Xi = \{\xi_1, \xi_2, \ldots, \xi_{n+p+1}\}$, where

n denotes the total number of basis functions. Using the know vector Ξ, b-spline basis functions are formed starting with the lowest degree $p = 0$ (piecewise constants) [75, 76]

$$N_{i,0}(\xi) = \begin{cases} 1 & \text{if} \quad \xi_i \leq \xi < \xi_{i+1} \,, \\ \\ 0 & \quad \text{otherwise} \,, \end{cases} \tag{11}$$

and, the higher-order b-spline basis functions, i.e., with $p > 0$, are constructed using

$$N_{i,p}(\xi) = \frac{\xi - \xi_i}{\xi_{i+p} - \xi_i} N_{i,p-1}(\xi) + \frac{\xi_{i+p+1} - \xi}{\xi_{i+p+1} - \xi_{i+1}} N_{i+1,p-1}(\xi) \,. \tag{12}$$

A B-spline curve $\mathscr{C}$ of order p can be represented via linear combinations of $N_{i,p}(\boldsymbol{\xi})$ with coefficients stored in a matrix $\boldsymbol{B}_i$ (of $\mathbb{R}^{n \times d}$), also referred to as the control points, using

$$\mathscr{C}(\xi) = \sum_{i=1}^{n} N_{i,p}(\xi) \boldsymbol{B}_i \tag{13}$$

in $\mathbb{R}^d$. The control points in $\boldsymbol{B}_i$ are adopted in lieu of nodal coordinates in the standard finite element (FE) context. However, b-splines are not interpolatory, whereas the nodal points (and fields) are generally interpolated in standard FE. For practical application of boundary conditions in the numerical analysis, an interpolatory b-spline curve at the ends is desired. To this end, we adopt *open* knot vectors and render physical domain with interpolated boundaries. The continuity of the p^{th} degree B-spline elements and their boundaries is of order $p - 1$, in the absence of repeated knots in the knot vector, achieving the highest possible smoothness for a given polynomial degree. Further details can be found in [76].

A b-spline surface can be constructed using the knot vector $\Xi = \{\xi_1, \xi_2, \ldots, \xi_{n+p+1}\}$ with the polynomial order p and the knot vector $H = \{\eta_1, \eta_2, \ldots, \eta_{m+q+1}\}$ with the polynomial order q. The surface $\mathscr{S}(\xi, \eta)$ is then represented as the product of the univariate b-splines

$$\mathscr{S}(\xi, \eta) = \sum_{j=1}^{m} \sum_{i=1}^{n} N_{i,p}(\xi) N_{j,q}(\eta) \boldsymbol{B}_{i,j} \,, \tag{14}$$

with the bidirectional control net $\boldsymbol{B}_{i,j}$. Essential to the isogeometric analysis, the same b-spline basis functions are used for the interpolation of the field variables, i.e., the bulk and the surface motion, $\boldsymbol{\varphi}$ and $\hat{\boldsymbol{\varphi}}$, respectively. The interpolations of the displacement field can be written as

$$\boldsymbol{\varphi}^{\boldsymbol{h}} = \boldsymbol{N}_l^p(\boldsymbol{\xi}_{\boldsymbol{b}})\boldsymbol{\varphi}^l \qquad \text{in} \quad \mathcal{B} \tag{15}$$

$$\boldsymbol{\varphi}^{\boldsymbol{h}} = \hat{\boldsymbol{N}}_m^p(\boldsymbol{\xi}_{\boldsymbol{s}})\boldsymbol{\varphi}^m \qquad \text{on} \quad \partial\mathcal{B}\,, \tag{16}$$

using the displacement field $\boldsymbol{\varphi}^l$ at the l^{th} *bulk* control point and $\boldsymbol{\varphi}^m$ for the m^{th} *surface* control point. $\boldsymbol{N}_i^p$ is a b-spline function of arbitrary degree p constructed from knot vectors defined in each parametric direction in two-dimensions. The enforced two-dimensionality is due to the axisymmetric assumptions. The polynomial degrees p and the knot vectors (parametric coordinates) of the bulk $\boldsymbol{\xi}_{\boldsymbol{b}} = \{\xi, \eta\}$ and of the surface $\boldsymbol{\xi}_{\boldsymbol{s}} = \{\xi\}$ match at the boundary such that $\boldsymbol{N}_l^{p\times p}(\boldsymbol{\xi}_{\boldsymbol{b}}) = \hat{\boldsymbol{N}}_l^p(\boldsymbol{\xi}_{\boldsymbol{s}}) \otimes \hat{\boldsymbol{N}}_l^p(\boldsymbol{\xi}_{\boldsymbol{s}})$ making use of tensor product nature of multivariate b-splines. The $(p{+}1)$ and $(p{+}1)\times(q{+}1)$ Gauss integration points are used for boundary (axisymmetric curve) and bulk elements, respectively.

Remark on the advantages of IGA: Note that it is, in principle, possible to approach this problem using standard FEM approaches such as the one adopted by Henann & Bertoldi [35] using Abaqus in combination with arclength (Riks) method. We took a different path and implemented our own in-house code using isogeometric analysis due to the various advantages that it provides. One advantage of IGA lies in its superior performance in approximating the solution compared to the standard FEM due to its high-order regularity. This results in higher accuracy per-degrees-of-freedom compared to FEM. Another advantage, when the domain is quasi-compressible, is that higher order elements significantly reduce the volumetric locking issues, without recourse to the F-bar method for the underlying bulk elements. Last but not least, one interesting example relevant to elastocapillary is accounting for flexural resistance of the surface [41]. The calculation of surface curvature tensor requires solving higher order equations and demands at least C^1-continuity of the spatial discretization that can be readily achieved in IGA.

3. Results and discussions

For the incompressible limit, only volume preserving deformations in bulk are permissible, excluding the behaviors of a large class of compressible materials and their associated P–R instability, e.g., see [77] for compressible behavior of hydrogels at relevant length-scales. The objective of this section is to quantify the role of compressiblity on the onset and the post-bifurcation behaviors for the solid P–R instability. First, we carry out an in-depth instability analysis of onset for the solid cylinder subjected to an increasing surface tension γ and applied end-stretches λ_L in Section 3.1. In this section, we present stability maps for stable-unstable behaviors considering two commonly used compressible strain energy functional, logarithmic- and quadratic-type, detailed in Eq. (8), over a range of (instantaneous) Poisson's ratios. Next, in Section 3.2, we focus on the post-instability behaviors and track the bifurcated branches after the onset using an arc-length-based numerical methodology. Although dynamic solutions [69] exist capturing the post-instability behavior, the full equilibrium path with stable-unstable branches have not been presented before. Our results clearly show the discontinuous nature of the instability, requiring the boundary to relax so as to follow the snap-back path.

Prior to and after the onset of the P–R instability, the deformations remain axisymmetric. The axial section of the cylinder and the boundary conditions are shown in Fig. 2. The cylinder geometry has dimensions of $R = 1$ and $L = 40$. The end boundaries of the geometry is constrained in the longitudinal direction, but free to move in the radial direction. We discretize this domain and its boundary with quadratic C^1-continuous B-spline elements. We first form the coarsest mesh, i.e., a single element, using the open knot vectors $\Xi = [0, 0, 0, 1, 1, 1]$ and $\mathcal{H} = [0, 0, 0, 1, 1, 1]$ and the polynomial degrees $p = q = 2$. Then, we perform uniform knot insertions (h−refinement) to obtain 25×1000 C^1-continuous axisymmetric bulk elements. The surface is directly partitioned from the bulk discretization with a matching curve parameterization. To this end, we construct 1000 C^1-continuous axisymmetric surface elements. In our simulations, the bulk material has the shear modulus $\mu = 1$ and we define the (dimensionless) elastocapillary number $\Gamma := \gamma/\mu R$ for later results. In the numerical simulations, depending on the study of interest, we either apply surface tension γ at fixed end-stretches or apply end-stretches at fixed surface tension.

3.1. Effect of compressibility on the onset of the solid P–R instability

In this section, we quantify the critical conditions for the mechanical stability of the compressible cylindrical employing two different compressible strain energy functionals for various Poisson's ratios. We first apply a prestretch λ_L to the cylinder in the longitudinal direction. Then, the surface tension on the boundary is increased until the onset of the instability. Figure 5 illustrates our numerical results pinpointing the critical surface tension γ at end-stretches $\lambda_L \in [0.6, 4]$ for the range of Poisson's ratio $\nu \in [0, 0.499]$. What stands out in this figure is the dominant effect of compressibility, i.e., both the Poisson's ratio as well as the type of compressible constitutive relations. Toward the incompressible limit, our results (e.g., for $\nu = 0.499$), as expected, approach the reported theoretical solution for an incompressible solid cylinder [58] (with $L_{ec}/R = 40$). This observation is valid for both strain energy densities of logarithmic-type (Fig. 5A) and quadratic-type (Fig. 5B). As the Poisson's ratio decreases, $\nu \to 0$, and the bulk becomes increasingly compressible, the solid cylinder remains stable at large stretches. Interestingly, using the quadratic-type strain energy model, we observe that the solid cylinder remains stable in parts where the simulations using logarithmic-type strain energy predicts P–R instability. This emphasizes on the importance of the proper selection of the volumetric part of the energy functional to study the P–R instability in compressible materials. At the compressible limit, both logarithmic- and quadratic-type strain energies display a closely matching behavior. Closer inspection of Fig. 5 shows

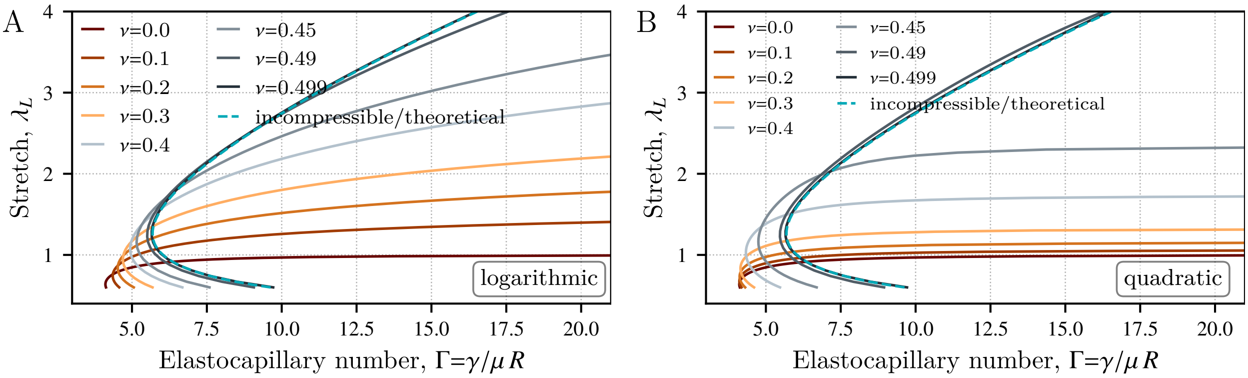

Figure 5: Stability maps obtained by increasing the surface tension, at fixed end-stretches, to the critical point where the P–R instability is detected through an eigenvalue analysis. The critical curves are obtained for various Poisson's ratios employing a logarithmic-type (**A**) and quadratic-type (**B**) strain energy densities. The dashed (green) line is a closed-form solution, i.e., Eq. (39) in [59], for an incompressible cylinder domain.

that, for fully compressible cylinders, the solid P–R instability is suppressed for the applied end-stretches $\lambda_L \lesssim 1$ for both logarithmic- and quadratic-type energy functional.

For each critical curve in Fig. 5, there exist a minimum critical elastocapillary number Γ, below which the cylinder remains stable independent of the applied overall stretch. There also exist a stretch λ_L that corresponds to the minimum critical Γ. To this end, Fig. 6A&B illustrate the minimum critical Γ and the corresponding end-stretch λ_L, respectively, over a range of compressibility, i.e., Poisson's ratio, for both logarithmic- and quadratic-type strain energy densities. For both energy types, we observe a decrease in the minimum critical Γ as the Poisson's ratio decreases. This behavior can be considered as a destabilizing effect of compressiblity. The minimum critical Γ is located at $(\lambda_L, \Gamma_{\text{crit}}) = (2^{\frac{1}{3}}, \sqrt{32})$ for a truly incompressible material, as predicted by weakly nonlinear stability analysis [58, 67]. Importantly, a sharp decrease in the critical Γ is observed in the quasi-compressible region where $\nu \in [0.4, 0.499]$. For the quadratic-type energy, the sharp decrease further continues and it reaches a

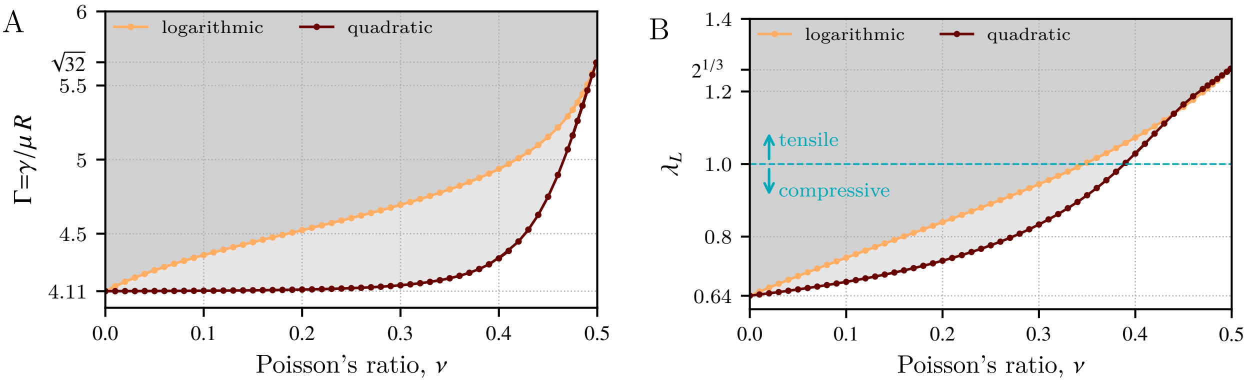

Figure 6: The minimum points in each critical stability curve is determined over the range of compressibility. The shaded area corresponds to the unstable P–R behavior. (**A**) Minimum critical elastocapillary number Γ for different Poisson's ratios is illustrated. (**B**) The corresponding applied stretch values can be compressive or tensile to achieve the minimum critical Γ.

plateau at compressible regime ($\nu < 0.3$). At the fully compressible limit, both strain energy types coincide at $(\lambda_L, \Gamma_{\text{crit}}) \approx (0.64, 4.11)$. This is expected because the penalty term of free energy densities vanishes since the Lamé parameter $\lambda = 0$. Hence, the overall energy densities in Eq. (8) recover the same form for both the logarithmic- and the quadratic-types. For the corresponding applied pre-stretches shown in Fig. 6B, we observe a steady decrease from 26% stretch at the incompressibility limit to 36% compression for at the fully compressible limit for both energy density types.

Let us now consider the case where λ_L=1 (no applied-stretch) and study the stability of the compressible solid cylinder subjected to an increasing surface tension. The stability map of the cylinder is illustrated in Fig. 7 for both quadratic- and logarithmic type strain energies for various Poisson's ratio. The critical curves divide the parameter space into two distinct regions: stable and unstable (shaded area). Again, at the incompressibility limit, we approach the theoretical solution of $\Gamma = 6$ reported in [15, 58]. As the domain becomes compressible, the critical Γ first decreases reaching a minimum and then sharply increases. The results of this investigation show that compressibility can have both stabilizing and destabilizing effect on the onset of P–R instability at fixed stretches. Toward the fully compressible regime, the required surface tension to trigger the P–R instability becomes far too large. This can be explained by the fact that the P–R instability is due to a competition between the bulk and surface energies. The surface tension applied on the boundary will deform the cylinder so as to minimize its surface area at fixed stretches by shrinking the radius in the radial direction (see Fig. 7B). This deformation causes mainly a volumetric change in the bulk. However, for fully compressible materials, the bulk shows no resistance against the surface-induced forces and shrinks uniformly to a thinner cylinder so as to minimize the surface area. This explains why the P–R instability is suppressed for fully compressible case at a fixed stretch. We have elucidated the influence of compressibility on the

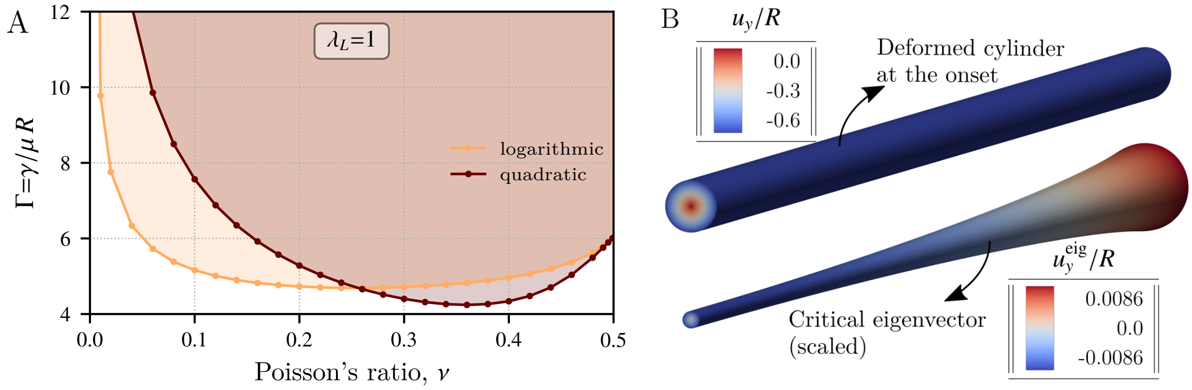

Figure 7: Compressibility has a pronounced effect on the onset of P–R instability. (**A**) The critical Γ over Poisson's ratios $\nu \in [0, 0.499]$ is shown for fixed boundaries, i.e., no-stretch case (λ_L=1). (**B**) The deformed geometry is plotted just before the instability initiates, i.e., at the onset. The contraction in the lateral direction is due to the increasing surface tension. At the onset, the critical eigenvalue-eigenvector pair is obtained for the minimum eigenvalue $\lambda^{\text{eig}} \approx 10^{-12}$. This is a qualitatively representative behavior for all other critical points.

onset of P–R instabilities. Moving forward, we illustrate the effect of compressibility on the post-instability quantities.

3.2. *Post-instability behavior of compressible P–R instability*

So far our analysis has only determined the onset of the instability, resulting in critical curves shown in Figs. 5 to 7. In this section, we characterize the type of bifurcations and also quantify the evolution of the instability beyond the critical points, from uniform cylinder geometry to the fully developed, beaded state. Recent theoretical studies [66] show that the solid P–R problem demonstrates a *snap-through* instability under increasing surface tension. This behavior is associated with the softening of reaction forces, leading to non-convex force-displacement curves. Similarly, we investigate the *snap-back* behavior of solid cylinders subjected to finite end-stretches at fixed surface tension. To this end, the post-bifurcation analyses is challenged by the discontinuous (subcritical) characteristics of the snap-back behavior and the simulation technique further requires a path-following nonlinear solution scheme, e.g., the arc-length method. In this section, we combine our axisymmetric, surface-enriched isogeometric formulation with an arclength solver employing the load parameter of applied end-stretch, λ_L. The path-following scheme first pinpoints the bifurcation point at what overall end-stretch the onset of instability occurs. Then, using the critical eigenvector at the onset, we use branch-switching to follow the equilibrium path [78]. Equipped with this efficient, path-following numerical scheme that can track stable-unstable states in the equilibrium path, in what follows, we will focus on the post-instability behavior of solid P–R problem at fixed elastocapillary number Γ.

Figure 8A illustrates the critical curve for the Poisson's ratio of $\nu = 0.4$ employing the quadratic-type strain energy potential. In this stability diagram, the shaded area corresponds to the unstable state, where a beading formation is observed in the post-bifurcation analysis. We present two possible scenarios. First, the points $a-e$ in Fig. 8 correspond

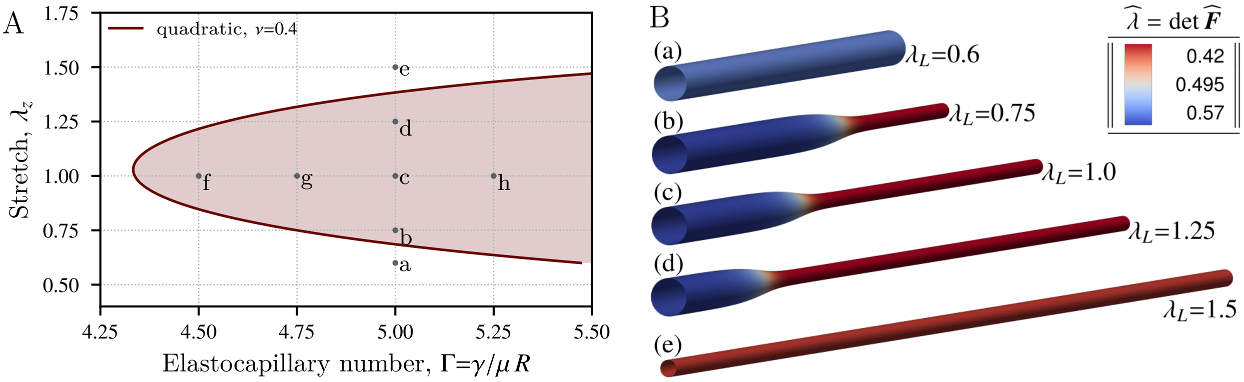

Figure 8: (**A**) The critical curve divides the domain into stable vs. unstable regions. The unstable domain is shown as shaded. The points $a-e$ corresponds to the simulations at fixed elastocapillary number $\Gamma = 5$. The points $fgch$ are at constant overall stretch $\lambda_L = 1$. (**B**) The three-dimensional deformed surface geometry, constructed from the axisymmetric solutions, are obtained at various stretch values at constant elastocapillary number $\Gamma = 5$. The colorbar corresponds to the determinant of the surface deformation gradient.

to the pre- and post-bifurcation behavior at constant elastocapillary number $\Gamma = 5$. Second, the points $fgch$ correspond to the simulation results at various elastocapillary values with fixed ends, i.e., no applied end-stretch λ_L=1.

The deformed geometry for both scenarios are shown in Fig. 8B, Figs. 9 and 10. The colormap in Figs. 9 and 10

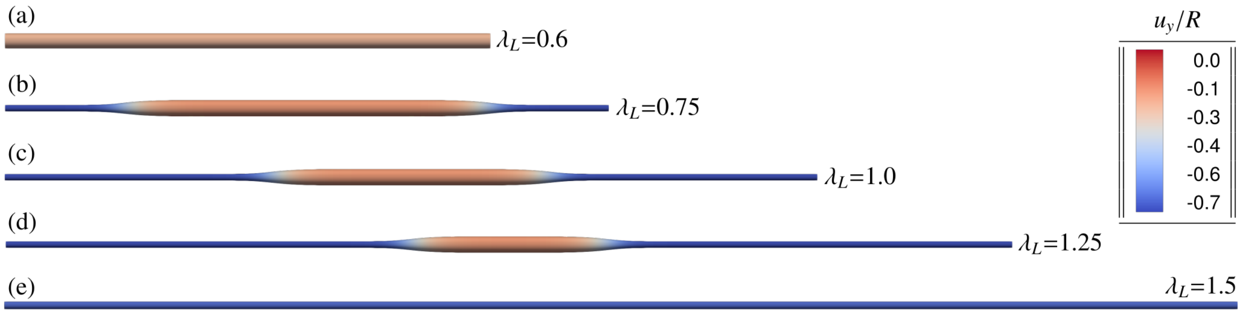

Figure 9: Deformed shapes corresponding to the points *abcde* in Fig. 8. The amplitude of the cylinder-like beading remains constant under applied stretch at the fixed elastocapillary number $\Gamma = 5$.

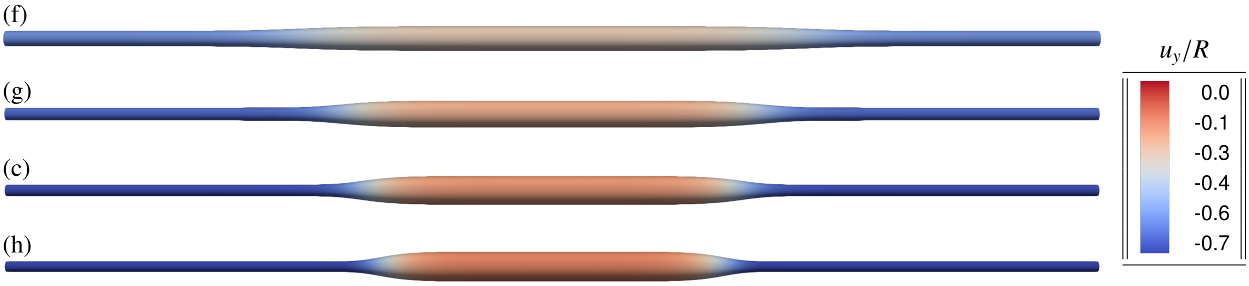

Figure 10: Deformed shapes corresponding to the points $fgch$ in Fig. 8. The surface tension is increasing from $f - g$ at fixed boundary conditions. A cylinder-like beading forms, which is also observed in experiments using soft polymeric gels [15].

illustrates the normalized radial displacements u_y/R. The following conclusions can be drawn from the present study. As shown in Fig. 9, the amplitude of the P–R instability remain the same from $b-d$ whereas the width of the cylinder-like beading decreases with increasing end-stretch. Eventually, the cylinder-like beading formation vanishes and a uniformly stretched cylinder is recovered (see Fig. 9e). The points a and e correspond to a homogeneous cylinder geometry and both points lie outside of the shaded area, further verifying the phase diagram shown in Fig. 8. We observe the separation of the cylinder into two distinct radii. This interesting result is attributed to a phase-separation-like behavior [69]. The phase-separated radii (into $r_{\max}$ and $r_{\min}$) and hence the amplitude ($a = r_{\max} - r_{\min}$) of the cylinder-like beading remain constant at increasing end-stretches throughout the unstable domain (shaded area in Fig. 8).

Let us now consider the second scenario, the points $fgch$ are obtained at fixed domain length where the surface is subjected to increasing surface tension (see Fig. 10). The deformations observed clearly indicates the energetic competition between the capillary forces and the hyperelasticity. The increase in surface tension deforms the cylinder, resulting in experimentally observed cylinder-like beadings. This goemetry is also referred to as cylinders-on-a-string (COAS) formations [68]. At vanishing shear modulus, e.g., the case of liquids, we expect the bulge to resemble a spherical bead due to dominating surface tension.

The results of this investigation demonstrate a wide tunability of solid P–R instability characteristics (onset, amplitude, and width), achieved by varying the applied end-stretch and elastocapillary number Γ. Note that Γ can be altered by exclusively varying the surface tension γ, the shear modulus μ of the material, and the initial radius R of the cylinder. The material behavior, in particular the type of the strain energy function, also plays a role in further enriching the tunability of P–R characteristics. Although both strain energy types investigated displayed qualitatively similar results (omitted for the sake of conciseness), the results obtained differed quantitatively in the compressible regime.

Next, we demonstrate the effect of different compressible strain energies on the instability characteristics, specifically using the quadratic- and logarithmic-types in Fig. 11.

Figure 11AB illustrates the change in maximum and minimum radii of the cylinder undergoing shape changes due to P–R instability for the quadratic-type and logarithmic-type strain energies, respectively. A non-monotonic behavior in applied stretch λ_L is observed where, at times, the stretch is reversed and the domain is compressed so as to follow the loading path. Hence, we expect, in experiments and dynamic solutions, the amplitude of the P–R waves will snap to a finite value in an instance. The non-monoticity in loading is permitted in a path-following solution scheme. Interested readers can refer to [78, 79] and the references therein. Notice that a displacement-controlled solution strategy, in lieu of using the path-following scheme, is likely to lose numerical convergence just after the onset and therefore fail to simulate this complex behavior. The loading paths, tracking the transient formation of P–R instability, are illustrated for the logarithmic- (Fig. 11A) and quadratic-type (Fig. 11B) functional at a fixed elastocapillary number $\Gamma = 5$ for the Poisson's ratio $\nu = 0.4$. In our simulations, we first apply a pre-stretch of $\lambda_L = 0.6$ to the cylinder and later on the surface tension is linearly increased to $\Gamma = 5$ on the boundary. In Fig. 11AB, the arc-length load parameter λ_L monotonically increases until the first critical point (★) at state **i**. At this singularity point, the critical eigenvector shown in Fig. 7B, corresponding to the zero eigenvalue within machine precision, favors deforming the cylinder non-uniformly in the lateral direction. Hence, a secondary path branches off the primary path (shown in gray-dashed line in Fig. 11) at this critical point, resulting in an axisymmetric bulging deformations. The primary path, corresponding to the uniform extension of the cylinder, becomes less favorable energetically. The path-following algorithm switches to the secondary, yet still unstable state (dotted line), which is energetically preferred. Proceeding the first critical point (★), the deformations snap-back at a minimum λ_L (●) at state **ii** and undergo a large

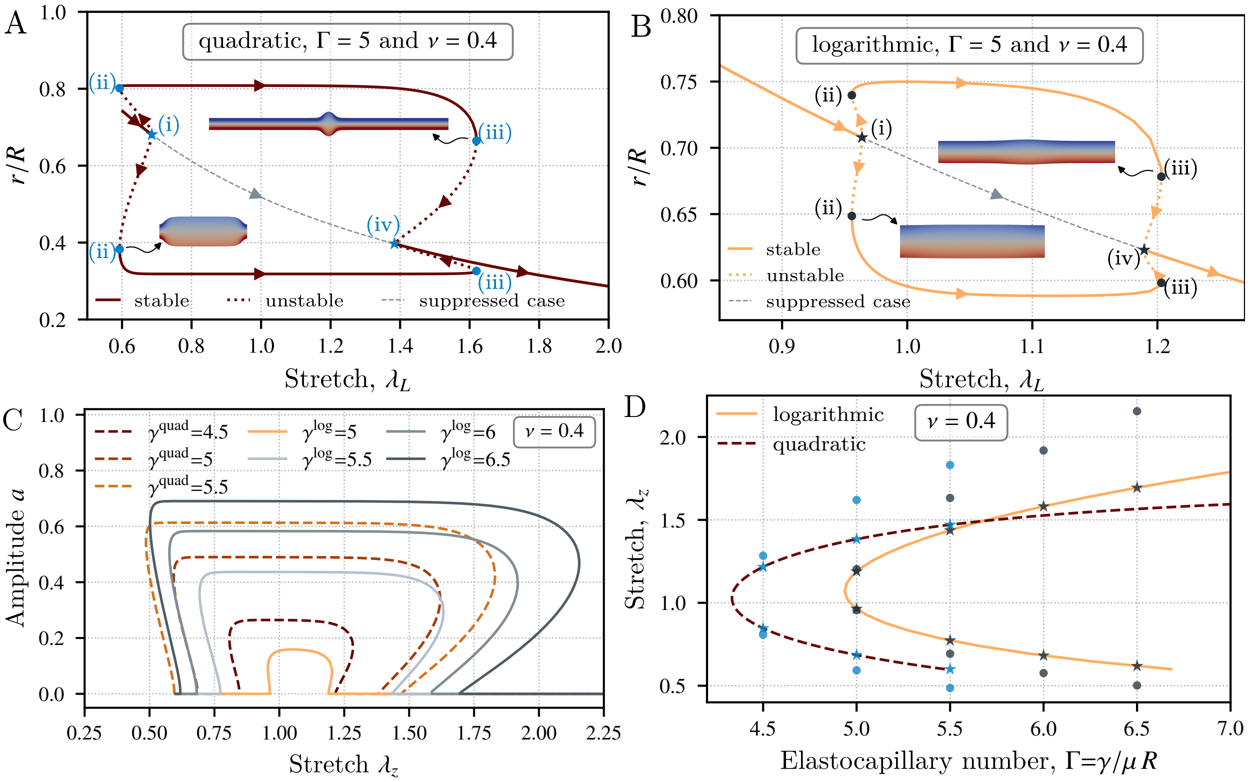

Figure 11: The evolution of minimum and maximum radii ($r_{\min}$ and $r_{\max}$) for simulations employing (**A**) quadratic and (**B**) logarithmic free energy densities for $\nu = 0.4$. The deformed shapes are shown as insets for the limit points (ii) and (iii). The deformations are amplified in the lateral direction by a factor of 10 for illustration purposes. For the bifurcation points (i) and (iv), the deformed shape is uniformly stretched cylinder. (**C**) The evolution of amplitude for various elastocapillary number and different strain energy types. (**D**) The bifurcation point are located on the critical curve whereas the limit points in the snap-back behavior are outside the critical curve.

amplitude growth forming a cylinder-like beading. Beyond this point, the path becomes stable and, surprisingly, the maximum and minimum radii remain roughly constant even though the overall stretch is increasing. Finally, the P–R instability eventually disappears when the applied stretch is large enough. Another snap-back behavior is observed between states **iii** and **iv**. At state **iv** (★), a uniformly stretched cylinder is recovered. Further increase in stretch contracts the radius of the cylinder without any bulging. The most interesting finding in Fig. 11 is that there is an interval of applied end-stretches where two states, i.e., a uniformly stretched cylinder and a beaded cylinder, coexist. Closer inspection of this figure reveals that the main deformations into cylinder-like bead formation take place during the snap-back portions. This behavior is associated with subcritical behaviors and it is known that such instabilities are highly sensitive to imperfections. Preexisting defects are expected to change the bifurcation-type instability into a limit-point instability, which can be efficiently tracked using the developed arclength method. A detailed study of defect-sensitivity of elastic P–R instability is interesting and it will be presented in a separate work. For the sake of conciseness, we restrict ourselves only to the homogeneous cylinder with perfect geometry.

Figure 11C illustrates the evolution of amplitude a calculated using $a = r_{\max} - r_{\min}$ for various Γ values. The larger the elastocapillary number Γ, the larger the amplitude grows during P-R instability. Unique to solid P–R problem, the amplitude remain constant between states ★**i** and ★**iv**. These states are located exactly on the critical curve presented earlier in Fig. 9 for quadratic-type strain energy and $\nu = 0.4$. Figure 11D illustrates these critical points ★ and the limit of snap-back behaviors (●) for both strain energy types. The bifurcation points ★ lie exactly on the critical curves whereas the limit points are outside the unstable region. Hence, we expect a premature onset or delayed disappearance under large end-stretches for the P–R in solid cylinders due to this metastable region. Notice that, as the elastocapillary number increases, the gap between the bifurcation and snap-back limit points increases. Closer to the minimum critical Γ, this gap is further reduced, i.e., snap-back behaviors with smaller intervals of unstable states are observed.

4. Conclusion

A slender solid cylinder subjected to surface tension on the boundary snaps into cylinder-like-beaded pattern due to an elastocapillary instability, i.e., the solid Plateau–Rayleigh instability. While a column of liquid breaks into spherical beads to minimize its overall surface area, the bulk elasticity resist the surface forces in solid cylinders. For surface stresses to deform the bulk, either the surface must be abundant or the bulk stiffness must be small enough to lead to an elastocapillary length $l_e = \gamma/\mu$ on the same order as the structural feature size. For thin fibers with shear modulus $\sim 10\,Pa$, the surface effects should be considered in fibers with radius of $O(1\text{ mm})$. To model surface stresses at such scales for soft fibers, we have implemented a surface-enriched isogeometric finite element framework at finite strains. A generic, formulation based on kinematic-energetic coupling is presented for compressible hyperelastic materials with boundaries in tension. Our framework is also capable of tracking structural stability and perform post-bifurcation analysis under complex, non-monotonic loads. This study has shown that material compressibility has significant effects on the onset and amplitude growth of the solid P–R patterns. In particular, both the Poisson's ratio and the form of volumetric strain energy have an influence. We quantified the compressible P–R instability characteristics comparing the two common type of compressible strain energies over a range of Poisson's ratios. Using a nonlinear path-following solution technique, we tracked the full equilibrium path including stable and unstable states. After the onset, under increasing stretch the radii at both ends of the cylinder remained constant with a short transition region. In potential experiments, we expect hysteresis in the loading and unloading path due to existence of metastable regions. The presented axisymmetric elastocapillary formulation proves to be an efficient and generic tool to study elastocapillary instabilities in polymeric soft solids. Our next immediate plan is to extend the current formulation to account for flexural resistance of the surface which is expected to introduce a bending length scale and regularize the P–R patterns.

Acknowledgment

AJ gratefully acknowledges the support provided by the Scientific and Technological Research Council of Turkey (TÜBITAK) Career Development Program, grant number 218M700. BD acknowledges funding from the National Science Foundation (NSF) through the DMREF program under grant number CMMI 2119716.

References

[1] C. W. Barney, C. E. Dougan, K. R. McLeod, A. Kazemi-Moridani, Y. Zheng, Z. Ye, S. Tiwari, I. Sacligil, R. A. Riggleman, S. Cai, J.-H. Lee, S. R. Peyton, G. N. Tew, A. J. Crosby, Cavitation in soft matter, Proceedings of the National Academy of Sciences 117 (2020) 9157–9165.

[2] R. W. Style, R. Boltyanskiy, B. Allen, K. E. Jensen, H. P. Foote, J. S. Wettlaufer, E. R. Dufresne, Stiffening solids with liquid inclusions, Nature Physics 11 (2015) 82–87.

[3] N. Kazem, M. D. Bartlett, C. Majidi, Extreme Toughening of Soft Materials with Liquid Metal, Advanced Materials 30 (2018) 1706594.

[4] J. Dervaux, M. Roché, L. Limat, Nonlinear theory of wetting on deformable substrates, Soft Matter 16 (2020) 5157–5176.

[5] B. Andreotti, J. H. Snoeijer, Soft wetting and the Shuttleworth effect, at the crossroads between thermodynamics and mechanics, EPL (Europhysics Letters) 113 (2016) 66001.

[6] J. B. Bostwick, M. Shearer, K. E. Daniels, Elastocapillary deformations on partially-wetting substrates: Rival contact-line models, Soft Matter 10 (2014) 7361–7369.

[7] W. Zhao, J. Zhou, H. Hu, C. Xu, Q. Xu, The role of crosslinking density in surface stress and surface energy of soft solids, Soft Matter 18 (2022) 507–513.

[8] J. T. Pham, F. Schellenberger, M. Kappl, H.-J. Butt, From elasticity to capillarity in soft materials indentation, Physical Review Materials 1 (2017) 015602.

[9] C.-Y. Hui, T. Liu, T. Salez, E. Raphael, A. Jagota, Indentation of a rigid sphere into an elastic substrate with surface tension and adhesion, Proceedings of the Royal Society A: Mathematical, Physical and Engineering Sciences 471 (2015) 20140727. doi:10.1098/rspa.2014.0727.

[10] T. Liu, R. Long, C.-Y. Hui, The energy release rate of a pressurized crack in soft elastic materials: Effects of surface tension and large deformation, Soft Matter 10 (2014) 7723–7729.

[11] D. P. Holmes, P.-T. Brun, A. Pandey, S. Protière, Rising beyond elastocapillarity, Soft Matter 12 (2016) 4886–4890.

[12] Q. Liu, T. Ouchi, L. Jin, R. Hayward, Z. Suo, Elastocapillary Crease, Physical Review Letters 122 (2019) 098003.

[13] S. Heyden, P. M. Vlahovska, E. R. Dufresne, A robust method for quantification of surface elasticity in soft solids, Journal of the Mechanics and Physics of Solids 161 (2022) 104786. doi:10.1016/j.jmps.2022.104786.

[14] M. R. Zafar, S. Basu, Calibrating surface hyperelastic constitutive models in soft solids, Physical Review E 103 (2021) 063003. doi:10.1103/PhysRevE.103.063003.

[15] S. Mora, T. Phou, J.-M. Fromental, L. M. Pismen, Y. Pomeau, Capillarity Driven Instability of a Soft Solid, Physical Review Letters 105 (2010) 214301.

[16] L. E. Scriven, Dynamics of a fluid interface Equation of motion for Newtonian surface fluids, Chemical Engineering Science 12 (1960) 98–108.

[17] M. E. Gurtin, A. Ian Murdoch, A continuum theory of elastic material surfaces, Archive for Rational Mechanics and Analysis 57 (1975) 291–323.

[18] P. Sharma, S. Ganti, N. Bhate, Effect of surfaces on the size-dependent elastic state of nano-inhomogeneities, Applied Physics Letters 82 (2003) 535–537.

[19] R. Dingreville, J. Qu, Mohammed Cherkaoui, Surface free energy and its effect on the elastic behavior of nano-sized particles, wires and films, Journal of the Mechanics and Physics of Solids 53 (2005) 1827–1854.

[20] J. He, C. M. Lilley, Surface effect on the elastic behavior of static bending nanowires, Nano Letters 8 (2008) 1798–1802.

[21] H. L. Duan, J. Wang, B. L. Karihaloo, Theory of Elasticity at the Nanoscale, Advances in Applied Mechanics 42 (2009) 1–68.

[22] A. Javili, A. McBride, P. Steinmann, Thermomechanics of solids with lower-dimensional energetics: On the importance of surface, interface, and curve structures at the nanoscale. A unifying review, Applied Mechanics Reviews 65 (2013) 010802.

[23] J. Yvonnet, H. L. Quang, Q. C. He, An XFEM/level set approach to modelling surface/interface effects and to computing the size-dependent effective properties of nanocomposites, Computational Mechanics 42 (2008) 119–131.

[24] A. Javili, A. Mcbride, J. Mergheim, P. Steinmann, U. Schmidt, Micro-to-macro transitions for continua with surface structure at the microscale, International Journal of Solids and Structures 50 (2013) 2561–2572.

[25] A. Javili, G. Chatzigeorgiou, A. T. McBride, P. Steinmann, C. Linder, Computational homogenization of nano-materials accounting for size effects via surface elasticity, GAMM Mitteilungen 38 (2015) 285–312.

[26] H. S. Park, P. A. Klein, G. J. Wagner, A surface Cauchy-Born model for nanoscale materials, International Journal for Numerical Methods in Engineering 68 (2006) 1072–1095.

[27] H. S. Park, P. A. Klein, A Surface Cauchy-Born model for silicon nanostructures, Computer Methods in Applied Mechanics and Engineering 197 (2008) 3249–3260.

[28] J. Yvonnet, A. Mitrushchenkov, G. Chambaud, Q. C. He, Finite element model of ionic nanowires with size-dependent mechanical properties determined by ab initio calculations, Computer Methods in Applied Mechanics and Engineering 200 (2011) 614–625.

[29] D. Davydov, A. Javili, P. Steinmann, On molecular statics and surface-enhanced continuum modeling of nano-structures, Computational Materials Science 69 (2013) 510–519.

[30] P. H. Saksono, D. Perić, On finite element modelling of surface tension Variational formulation and applications - Part I: Quasistatic problems, Computational Mechanics 38 (2006) 265–281.

[31] P. H. Saksono, D. Perić, On finite element modelling of surface tension: Variational formulation and applications - Part II: Dynamic problems, Computational Mechanics 38 (2006) 251–263.

[32] R. Brown, F. Orr, L. Scriven, Static drop on an inclined plate: Analysis by the finite element method, Journal of Colloid and Interface Science (1980) 76–87.

[33] A. Javili, P. Steinmann, A finite element framework for continua with boundary energies. Part I: The two-dimensional case, Computer Methods in Applied Mechanics and Engineering 198 (2009) 2198–2208.

[34] A. Javili, P. Steinmann, A finite element framework for continua with boundary energies. Part II: The three-dimensional case, Computer Methods in Applied Mechanics and Engineering 199 (2010) 755–765.

[35] D. L. Henann, K. Bertoldi, Modeling of elasto-capillary phenomena, Soft Matter 10 (2014) 709–717.

[36] Y. Wang, D. L. Henann, Finite-element modeling of soft solids with liquid inclusions, Extreme Mechanics Letters 9 (2016) 147–157.

[37] S. Mora, C. Maurini, T. Phou, J.-M. Fromental, B. Audoly, Y. Pomeau, Solid Drops: Large Capillary Deformations of Immersed Elastic Rods, Physical Review Letters 111 (2013) 114301.

[38] J. He, H. S. Park, A methodology for modeling surface effects on stiff and soft solids, Computational Mechanics 61 (2018) 687–697.

[39] S. Seifi, H. S. Park, Electro-elastocapillary Rayleigh-plateau instability in dielectric elastomer films, Soft Matter 13 (2017) 4305–4310.

[40] R. W. Style, A. Jagota, C.-Y. Hui, E. R. Dufresne, Elastocapillarity: Surface Tension and the Mechanics of Soft Solids, Annual Review of

Condensed Matter Physics 8 (2017) 99–118.

[41] D. J. Steigmann, R. W. Ogden, Elastic surface-substrate interactions, Proceedings of the Royal Society A: Mathematical, Physical and Engineering Sciences 455 (1999) 437–474.

[42] A. I. Murdoch, A thermodynamical theory of elastic material interfaces, Quarterly Journal of Mechanics and Applied Mathematics 29 (1976) 245–275.

[43] F. Dell'isola, A. Romano, On the derivation of thermomechanical balance equations for continuous systems with a nonmaterial interface, International Journal of Engineering Science 25 (1987) 1459–1468.

[44] E. Fried, M. E. Gurtin, Thermomechanics of the interface between a body and its environment, Continuum Mechanics and Thermodynamics 19 (2007) 253–271.

[45] A. Javili, S. Kaessmair, P. Steinmann, General imperfect interfaces, Computer Methods in Applied Mechanics and Engineering 275 (2014) 76–97.

[46] G. Chatzigeorgiou, F. Meraghni, A. Javili, Generalized interfacial energy and size effects in composites, Journal of the Mechanics and Physics of Solids 106 (2017) 257–282.

[47] A. Javili, P. Steinmann, J. Mosler, Micro-to-macro transition accounting for general imperfect interfaces, Computer Methods in Applied Mechanics and Engineering 317 (2017) 274–317.

[48] V. A. Lubarda, Rate-type elasticity and viscoelasticity of an erythrocyte membrane, Journal of Mechanics of Materials and Structures 6 (2011) 361–376.

[49] H. Altenbach, V. A. Eremeyev, N. F. Morozov, Surface viscoelasticity and effective properties of thin-walled structures at the nanoscale, International Journal of Engineering Science 59 (2012) 83–89.

[50] L. Liu, M. Yu, H. Lin, R. Foty, Deformation and relaxation of an incompressible viscoelastic body with surface viscoelasticity, Journal of the Mechanics and Physics of Solids 98 (2017) 309–329.

[51] R. A. Sauer, R. Ghaffari, A. Gupta, The multiplicative deformation split for shells with application to growth, chemical swelling, thermoelasticity, viscoelasticity and elastoplasticity, International Journal of Solids and Structures 174-175 (2019) 53–68.

[52] B. Dortdivanlioglu, A. Javili, Boundary viscoelasticity theory at finite deformations and computational implementation using isogeometric analysis, Computer Methods in Applied Mechanics and Engineering 374 (2021) 113579.

[53] J. Eggers, Nonlinear dynamics and breakup of free-surface flows, Reviews of Modern Physics 69 (1997) 865–930.

[54] J. Eggers, E. Villermaux, Physics of liquid jets, Reports on Progress in Physics 71 (2008) 036601.

[55] R. W. Style, A. Jagota, C.-Y. Hui, E. R. Dufresne, Elastocapillarity: Surface Tension and the Mechanics of Soft Solids, Annual Review of Condensed Matter Physics 8 (2017) 99–118. doi:10.1146/annurev-conmatphys-031016-025326.

[56] J. Bico, É. Reyssat, B. Roman, Elastocapillarity: When Surface Tension Deforms Elastic Solids, Annual Review of Fluid Mechanics 50 (2018) 629–659. doi:10.1146/annurev-fluid-122316-050130.

[57] S. Mora, Y. Pomeau, Softening of edges of solids by surface tension, Journal of Physics: Condensed Matter 27 (2015) 194112.

[58] M. Taffetani, P. Ciarletta, Elastocapillarity can control the formation and the morphology of beads-on-string structures in solid fibers, Physical Review E 91 (2015) 032413. doi:10.1103/PhysRevE.91.032413.

[59] M. Taffetani, P. Ciarletta, Beading instability in soft cylindrical gels with capillary energy: Weakly non-linear analysis and numerical simulations, Journal of the Mechanics and Physics of Solids 81 (2015) 91–120.

[60] D. Riccobelli, Active elasticity drives the formation of periodic beading in damaged axons, Physical Review E 104 (2021) 024417. doi:10.1103/PhysRevE.104.024417.

[61] P. Ciarletta, M. Ben Amar, Peristaltic patterns for swelling and shrinking of soft cylindrical gels, Soft Matter 8 (2012) 1760.

[62] B. Barrière, K. Sekimoto, L. Leibler, Peristaltic instability of cylindrical gels, The Journal of Chemical Physics 105 (1996) 1735–1738.

[63] L. Wang, Axisymmetric instability of soft elastic tubes under axial load and surface tension, International Journal of Solids and Structures 191-192 (2020) 341–350.

[64] Q. Wang, M. Liu, Z. Wang, C. Chen, J. Wu, Large Deformation and Instability of Soft Hollow Cylinder With Surface Effects, Journal of Applied Mechanics 88 (2021) 041010.

[65] D. Emery, Y. Fu, Localised bifurcation in soft cylindrical tubes under axial stretching and surface tension, International Journal of Solids and Structures 219-220 (2021) 23–33.

[66] Y. Fu, L. Jin, A. Goriely, Necking, beading, and bulging in soft elastic cylinders, Journal of the Mechanics and Physics of Solids 147 (2021) 104250.

[67] C. Xuan, J. Biggins, Finite-wavelength surface-tension-driven instabilities in soft solids, including instability in a cylindrical channel through an elastic solid, Physical Review E 94 (2016) 023107. doi:10.1103/PhysRevE.94.023107.

[68] A. Pandey, M. Kansal, M. A. Herrada, J. Eggers, J. H. Snoeijer, Elastic Rayleigh–Plateau instability: Dynamical selection of nonlinear states, Soft Matter 17 (2021) 5148–5161.

[69] C. Xuan, J. Biggins, Plateau-Rayleigh instability in solids is a simple phase separation, Physical Review E 95 (2017) 053106. doi:10.1103/PhysRevE.95.053106.

[70] A. Giudici, J. S. Biggins, Ballooning, bulging, and necking: An exact solution for longitudinal phase separation in elastic systems near a critical point, Physical Review E 102 (2020) 033007.

[71] C. Lestringant, B. Audoly, A diffuse interface model for the analysis of propagating bulges in cylindrical balloons, Proceedings of the Royal Society A: Mathematical, Physical and Engineering Sciences 474 (2018) 20180333. doi:10.1098/rspa.2018.0333.

[72] C. Lestringant, B. Audoly, A one-dimensional model for elasto-capillary necking, Proceedings of the Royal Society A: Mathematical, Physical and Engineering Sciences 476 (2020) 20200337.

[73] S. I. Tamim, J. B. Bostwick, Plateau–Rayleigh instability in a soft viscoelastic material, Soft Matter (2021).

[74] T. J. R. Hughes, J. A. Cottrell, Y. Bazilevs, Isogeometric analysis: CAD, finite elements, NURBS, exact geometry and mesh refinement, Computer Methods in Applied Mechanics and Engineering 194 (2005) 4135–4195.

[75] J. A. Cottrell, T. J. Hughes, Y. Bazilevs, Isogeometric analysis: toward integration of CAD and FEA, John Wiley & Sons, 2009.

[76] L. Piegl, W. Tiller, The NURBS Book, Monographs in Visual Communication, Springer-Verlag, Berlin Heidelberg, 1995.

[77] J. Cappello, V. d'Herbemont, A. Lindner, O. du Roure, Microfluidic In-Situ Measurement of Poisson's Ratio of Hydrogels, Micromachines 11 (2020) 318. doi:10.3390/mi11030318.

[78] P. Wriggers, Solution Methods for Time Independent Problems, in: Nonlinear Finite Element Methods, Springer, pp. 149–204.

[79] M. A. Crisfield, A fast incremental/iterative solution procedure that handles "snap-through", in: A. K. Noor, H. G. McCOMB (Eds.), Computational Methods in Nonlinear Structural and Solid Mechanics, Pergamon, 1981, pp. 55–62.